PERGAMON

Computers & Fluids 29 (2000) 725–748

computers & fluids

www.elsevier.com/locate/compfluid

A gas-kinetic scheme for reactive flows

Yongsheng Lian, Kun Xu*

Department of Mathematics, Hong Kong University of Science and Technology, Clear Water Bay, Kowloon, Hong Kong

Received 23 November 1998; received in revised form 22 July 1999; accepted 22 July 1999

Abstract

In this paper, the gas-kinetic BGK scheme for the compressible flow equations is extended to chemical reactive flow. The mass fraction of the unburnt gas is implemented into the gas kinetic formulation by assigning a new internal degree of freedom to the particle distribution function. This new variable can be also used to describe fluid trajectory for the nonreactive flows. The gas-kinetic BGK model basically solves the Navier–Stokes chemical reactive flow equations. Numerical examples validate the accuracy and robustness of the current approach.

1. Introduction

There are many numerical approaches to the solution of the compressible Euler equations. The Godunov and the Boltzmann schemes are two of them. Broadly speaking, the Godunov scheme is based on the Riemann solution and characteristics plays an important role in the description of gas evolution. The Boltzmann scheme uses the microscopic particle distribution function as the basis in the construction of flux function and the Euler solution is considered as a limiting case as the fluid stays in an equilibrium state. The Godunov and the Boltzmann schemes are based on two different physical interpretations of flow motion. With the possible adaptation of nonequilibrium gas property in the kinetic scheme, the robustness of the scheme is obtained in the discontinuity flow regions and the accuracy of the scheme in the smooth region can be also improved with the correct implementation of particle collisions in the gas evolution stage [18].

* Corresponding author. Tel.: +852-2358-7433; fax: +852-2358-1643.
E-mail address: makxu@uxmail.ust.hk (K. Xu).

0045-7930/00/$ - see front matter
PII: S0045-7930(99)00034-1

In this paper, we extend the gas-kinetic BGK scheme for the nonreactive compressible Euler equations to the reactive flows. In order to include the mass fraction into the kinetic formulation, one new internal degree of freedom z is introduced in the gas distribution function. For nonreactive flows, this function can be simply used for the tracking of fluid trajectory. In the current paper, only two species are considered, which are the unburnt and burnt gases. The unburnt gas is converted to burnt gas via a simple irreversible reaction process. As a special application, the new scheme is used in the simulation of detonation waves in both 1D and 2D cases [6].

The inviscid reacting compressible Euler equations in 1D case are

$$\begin{aligned}
&\rho_t + (\rho U)_x = 0,\\
&(\rho U)_t + \left(\rho U^2 + p\right)_x = 0,\\
&(\rho Z)_t + (\rho Z U)_x = -\rho K(T) Z,\\
&(\rho \epsilon)_t + (\rho \epsilon U + pU)_x = Q_0 \rho K(T) Z,
\end{aligned} \tag{1}$$

where ρ is the density, U is the velocity, p is the pressure, Z is the mass fraction of unburnt gas, and Q_0 is the amount of heat released per unit mass by reaction. The total energy density is $\rho\epsilon = \frac{1}{2}\rho U^2 + \rho e$ where ρe is the internal energy. We assume that both unburnt and burnt gases have the same γ.The equation of state can be expressed as $p = \rho RT$, where R is the gas constant. $K(T)$ is the chemical reactive rate, which is a function of temperature. The specific form of $K(T)$ will be given in the numerical section.

Many researchers have been working on the numerical solution of Eq. (1). A partial list of references include Colella et al. [3], Lindstrom [12], Engquist and Sjogreen [4], and Jeltsch and Klingenstein [9]. Basically, a splitting scheme is used to solve the above equations and the cell-averaged flow variables $W_j = (\rho, \rho U, \rho Z, \rho\epsilon)_j^{\mathrm{T}}$ inside each cell are updated through

$$\frac{\mathrm{d}W_j}{\mathrm{d}t} = \frac{1}{\Delta x}\left(F_{j-1/2}(t) - F_{j+1/2}(t)\right) + S\left(W_j\right),$$

where $S = (0,\ 0,\ -\rho K(T)Z,\ Q_0 \rho K(T) Z)_j^{\mathrm{T}}$ is the source term and the flux function $F_{j+1/2}$ is obtained by solving Eq. (1) without considering the source effect. In this paper, a gas-kinetic model and the corresponding kinetic scheme for the evaluation of the numerical flux function will be presented. The source term $S(W_j)$ in the above equation is treated implicitly for the update of flow variables W_j inside each cell [16].

2. A gas-kinetic model

A gas-kinetic BGK model for Eq. (1) without the source terms on the right-hand side can be constructed as follows:

$$f_t + uf_x = \frac{g-f}{\tau}, \tag{2}$$

where f is the gas-distribution function, u the particle velocity, and $Q(f,f) = (g-f)/\tau$ the collision term [1]. The equilibrium state g has the form,

$$g = \rho\left(\frac{\lambda}{\pi}\right)^{(K+2)/2} \mathrm{e}^{-\lambda\left((u-U)^2+(z-Z)^2+\xi^2\right)},$$

where K is the number of dimensions of the internal variable ξ and is related to γ,

$$K = \frac{3-\gamma}{\gamma-1}$$

and $\xi^2 = \xi_1^2 + \xi_2^2 + \cdots + \xi_K^2$. The variable λ is a function of the gas temperature T with the relation $\lambda = m/2kT$, where k is the Boltzmann constant and m is the molecular mass.

The connection between the distribution function f and macroscopic flow variables is

$$(\rho, \rho U, \rho Z, \rho\epsilon)^{\mathrm{T}} = \int \psi_\alpha f \,\mathrm{d}u\,\mathrm{d}z\,\mathrm{d}\xi,$$

where $\mathrm{d}\xi = \mathrm{d}\xi_1\,\mathrm{d}\xi_2\cdots\mathrm{d}\xi_K$, and

$$\psi_\alpha = \left(1, u, z, \frac{1}{2}\left(u^2+\xi^2\right)\right)^{\mathrm{T}}$$

are the moments for density ρ, momentum ρU, mass fraction ρZ, and total energy $\rho\epsilon$. The fluxes in the x-direction for the corresponding macroscopic variables are

$$\left(F_\rho, F_{\rho U}, F_{\rho Z}, F_{\rho\epsilon}\right)^{\mathrm{T}} = \int u\psi_\alpha f \,\mathrm{d}u\,\mathrm{d}z\,\mathrm{d}\xi.$$

The compatibility condition for the BGK model (2) is

$$\int Q(f,f)\psi_\alpha \,\mathrm{d}u\,\mathrm{d}z\,\mathrm{d}\xi = \begin{pmatrix} 0 \\ 0 \\ 0 \\ 0 \end{pmatrix}. \tag{3}$$

With the equilibrium assumption $f = g$, the compressible Euler equations with the inclusion of mass fraction can be derived by taking the moments of ψ_α to Eq. (2),

$$\int \begin{pmatrix} 1 \\ u \\ z \\ \frac{1}{2}\left(u^2+\xi^2\right) \end{pmatrix} (g_t + ug_x)\,\mathrm{d}u\,\mathrm{d}z\,\mathrm{d}\xi = 0,$$

and the resulting equations are

$$\begin{pmatrix} \rho \\ \rho U \\ \rho Z \\ \frac{1}{2}\rho\left(U^2+\frac{K+1}{2\lambda}\right) \end{pmatrix}_t + \begin{pmatrix} \rho U \\ \rho U^2+\frac{\rho}{2\lambda} \\ \rho ZU \\ \frac{1}{2}\rho\left(U^3+\frac{(K+3)U}{2\lambda}\right) \end{pmatrix}_x = 0.$$

Here, the corresponding pressure is $p = \rho/2\lambda$ and the internal energy density ρe goes to

$$\rho e = \frac{(K+1)\rho}{4\lambda}.$$

To the first order of τ, the Chapman–Enskog expansion gives

$$f = g - \tau(g_t + ug_x),$$

and the BGK model automatically reduces to the Navier–Stokes equations,

$$\begin{pmatrix} \rho \\ \rho U \\ \rho Z \\ \frac{1}{2}\rho\left(U^2+\frac{K+1}{2\lambda}\right) \end{pmatrix}_t + \begin{pmatrix} \rho U \\ \rho U^2+\frac{\rho}{2\lambda} \\ \rho UZ \\ \frac{1}{2}\rho\left(U^3+\frac{(K+3)U}{2\lambda}\right) \end{pmatrix}_x$$

$$= \tau \begin{pmatrix} 0 \\ \frac{2K}{K+1}\frac{\rho}{2\lambda}U_x \\ \frac{\rho}{2\lambda}Z_x \\ \frac{K+3}{4}\frac{\rho}{2\lambda}\left(\frac{1}{\lambda}\right)_x + \frac{2K}{K+1}\frac{\rho}{2\lambda}UU_x \end{pmatrix}_x, \tag{4}$$

where the dynamic viscous coefficient is $\eta = \tau p$. In 2D cases, similar viscous governing equations can be derived from the BGK model [18]. As a result, for the chemical reactive flows,the real governing equations solved by the kinetic BGK scheme are the reactive Navier–Stokes equations instead of inviscid Eq. (1). This is one of the direct reason for the robustness of kinetic BGK scheme.

Remark. *In the above BGK model, the variable Z in the equilibrium state g has no dynamical effect on the gas evolution, it only provides additional information about the flow motion, which can be the mass fraction for the reactive flow, level set function for the interface tracking, color function for the fluid trajectory capturing, and the pollution concentration for different species.*

3. Gas-kinetic flow solver

In order to evaluate the numerical fluxes across a cell interface $x_{j+1/2}$, we need to evaluate the gas distribution function there.The general solution of f at the cell interface $x_{j+1/2}$ and time t is

$$f(x_{j+1/2}, t, u, z, \xi) = \frac{1}{\tau}\int_0^t g(x', t', u, z, \xi)\mathrm{e}^{-(t-t')/\tau}\,\mathrm{d}t' + \mathrm{e}^{-t/\tau}f_0(x_{j+1/2} - ut), \tag{5}$$

where $x' = x_{j+1/2} - u(t-t')$ is the trajectory of the particle motion and f_0 is the gas distribution function f at the beginning of each time step ($t = 0$). Two unknowns, g and f_0 in Eq. (5), have to be addressed in order to obtain the distribution function f.

Generally, the distributions of f_0 and g around the cell interface $x_{j+1/2}$ and time $t = 0$ are obtained using the Taylor expansion of the Maxwellian distribution function, such that

$$f_0 = \begin{cases} g^l\big(1 + a^l(x - x_{j+1/2})\big), & x \le x_{j+1/2} \\ g^r\big(1 + a^r(x - x_{j+1/2})\big), & x \ge x_{j+1/2} \end{cases}$$

and

$$g = g_0\Big(1 + \big(1 - H[x - x_{j+1/2}]\big)\bar{a}^l(x - x_{j+1/2}) + H[x - x_{j+1/2}]\bar{a}^r(x - x_{j+1/2}) + \bar{A}t\Big), \tag{6}$$

where g^{l}, g^{r} and g_0 are local Maxwellian distribution functions located at the left, right and middle of a cell interface.The parameters a^l, a^r, $\bar{a}^l$, $\bar{a}^r$ have the following form

$$a = a_1 + a_2u + a_3z + a_4\frac{u^2 + \xi^2}{2},$$

and all parameters (a_1, a_2, a_3, a_4) can be obtained from the slopes of the reconstructed macroscopic variables $\bar{W}_j(x)$ inside each cell. $H[x]$ is the Heaviside function defined as

$$H[x] = \begin{cases} 0, & x < 0 \\ 1, & x \ge 0 \end{cases}.$$

The reason and detailed formulation in the determination of f_0 is presented in [18,19]. The only difference here is that we need additionally use the macroscopic distribution ρZ in the determination of a_3z term.

The equilibrium state g_0 at a cell interface has the form

$$g_0 = \rho_0\left(\frac{\lambda_0}{\pi}\right)^{(K+2)/2}\mathrm{e}^{-\lambda_0\left((u-U_0)^2 + (z-Z_0)^2 + \xi^2\right)},$$

which is determined as follows. Taking the limit of $t \to 0$ in Eq. (5) and substituting its solution into Eq. (3), the compatibility constraint at ($x = x_{j+1/2}$, $t = 0$) gives

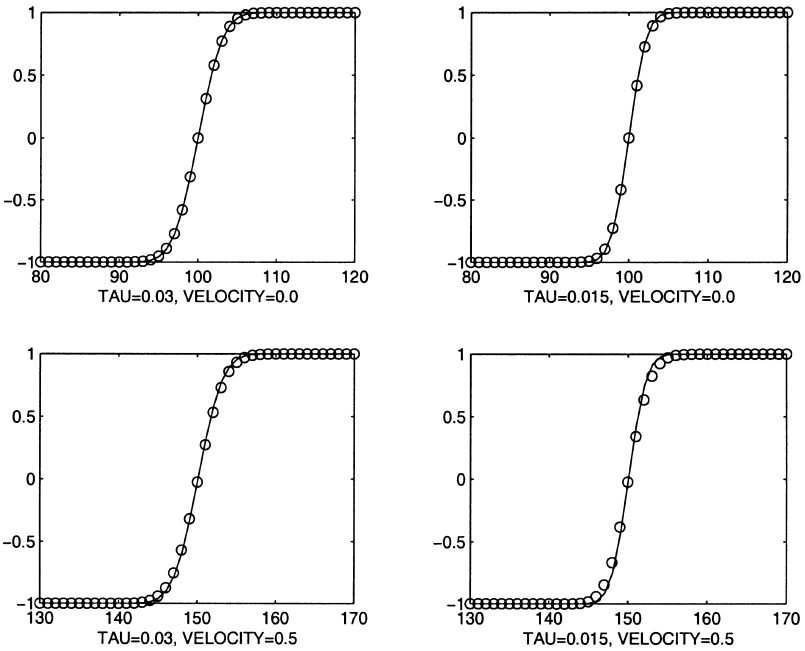

Fig. 1. Propagation of function Z with velocity $U = 0$ (top) and $U = 0.5$ (bottom). The collision times used are $\tau = 0.03$ (left) and $\tau = 0.015$ (right), respectively. The solid lines are exact solutions and the circles are numerical ones.

$$W_0 = \int g_0 \psi_\alpha \, du \, dz \, d\xi = \int_{u>0} \int g^l \psi_\alpha \, du \, dz \, d\xi + \int_{u<0} \int g^r \psi_\alpha \, du \, dz \, d\xi.$$

Similarly the corresponding slopes of ā in Eq. (6) can be obtained from the macroscopic slopes by connecting the cell averaged flow quantities W_j and W_{j+1} with the above obtained value W_0 at the cell interface [19].

After substituting Eq. (6) in Eq. (5), the final gas distribution function at a cell interface becomes

$$\begin{aligned} f(x_{j+1/2}, t, u, z, \xi) = {} & (1 - e^{-t/\tau}) g_0 + \tau \left(t/\tau - 1 + e^{-t/\tau} \right) \bar{A} g_0 \left(\tau \left(-1 + e^{-t/\tau} \right) + t e^{-t/\tau} \right) \\ & \times \left(\bar{a}^l H[u] + \bar{a}^r \left(1 - H[u] \right) \right) u g_0 + e^{-t/\tau} \Big((1 - uta^l) H[u] g^l + (1 - uta^r) \\ & \times \left(1 - H[u] \right) g^r \Big). \end{aligned} \tag{7}$$

The only unknown in the above equation is $\bar{A}$ term, which is determined subsequently by implementing the compatibility condition over the whole time step Δt at the location $x_{j+1/2}$,

$$\int_0^{\Delta t} \int \left(g(x_{j+1/2}, t, u, z, \xi) - f(x_{j+1/2}, t, u, z, \xi) \right) \psi_\alpha \, dt \, du \, dz \, d\xi = 0.$$

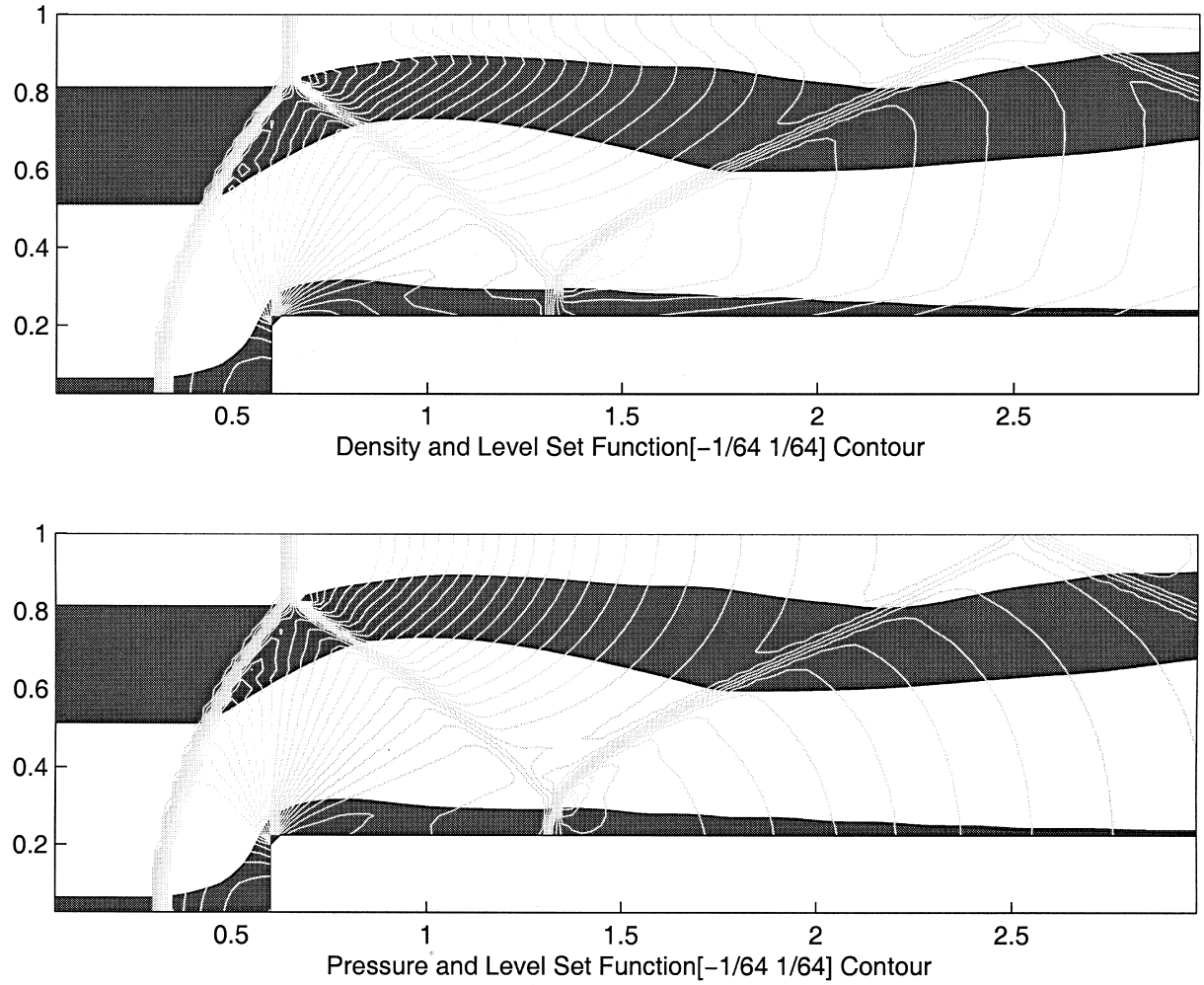

Fig. 2. Density and pressure contours. The shadowed regions represent the regions with different values of Z.

There is no iteration involved in the determination of $\bar{A}$ from the above equation. After f is obtained, the time-dependent numerical fluxes in the x-direction across the cell interface can be computed as

$$\begin{pmatrix} F_\rho \\ F_{\rho U} \\ F_{\rho Z} \\ F_{\rho\epsilon} \end{pmatrix}_{j+1/2} = \int u \begin{pmatrix} 1 \\ u \\ z \\ \frac{1}{2}(u^2+\xi^2) \end{pmatrix} f\left(x_{j+1/2}, t, u, z, \xi\right) \mathrm{d}u\, \mathrm{d}z\, \mathrm{d}\xi. \tag{8}$$

By integrating the above equation over the whole time step Δt, we get $W = (\rho, \rho U, \rho Z, \rho\epsilon)^{\mathrm{T}}$ transport in a whole time step.

Remark 1. *The detailed numerical formulation of the gas-kinetic BGK scheme is presented in [18,19]. Any one who is not familiar with the kinetic scheme can find reference [18] useful. Basically, the main difference between the current BGK method from the well-defined Kinetic Flux Vector Splitting (KFVS) Scheme [15,13] based on the collisionless Boltzmann equation is that the BGK scheme includes the particle collisions in the gas evolution stage. As a result, the viscosity and heat conduction coefficients in the BGK scheme are automatically decoupled from the numerical time step. The KFVS scheme keeps only* $f_0(x_{j+1/2} - ut)$ *term in Eq. (5) of the BGK formulation.*

Remark 2. *In comparison with the Godunov-type schemes based on the exact or approximate Riemann solvers, the kinetic BGK scheme is very robust and accurate. The main reason for this is that the BGK scheme is solving the viscous governing equations directly in both discontinuity and smooth regions, where the slopes of macroscopic variables inside each cell are used in the flux evaluation, instead of using only two pointwise values in the Godunov-type method. The efficiency of the BGK scheme is about 1 or 2 times slower than most upwinding schemes. The detailed comparison of computational cost between the BGK scheme and other popular Riemann solvers is listed in [10]. A simplified version of BGK-type scheme is obtained by Kotelnikov and Montgomery in [11].*

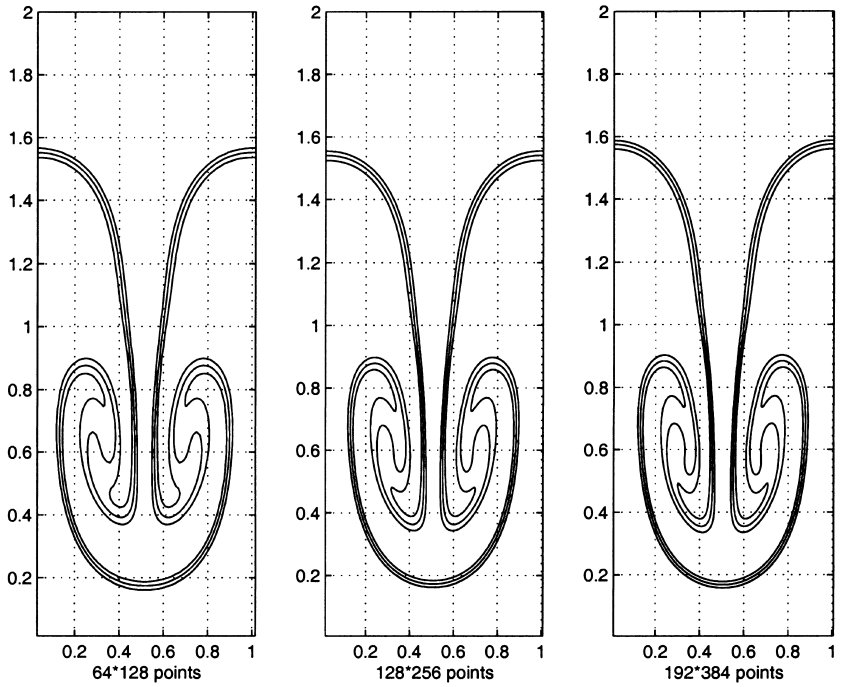

Fig. 3. Rayleigh–Taylor instability. The interface between the heavy and light fluid is captured with the help of function Z, and the lines with the values of $Z = [-0.5, 0.0, 0.5]$ are plotted. From left to right, the mesh sizes used are 64×128, 128×256, 192×384 and the collision time keeps the same value $\tau = 4 \times 10^{-4}$ in all cases. Therefore, the physical viscous coefficient is the same, so are the simulation results.

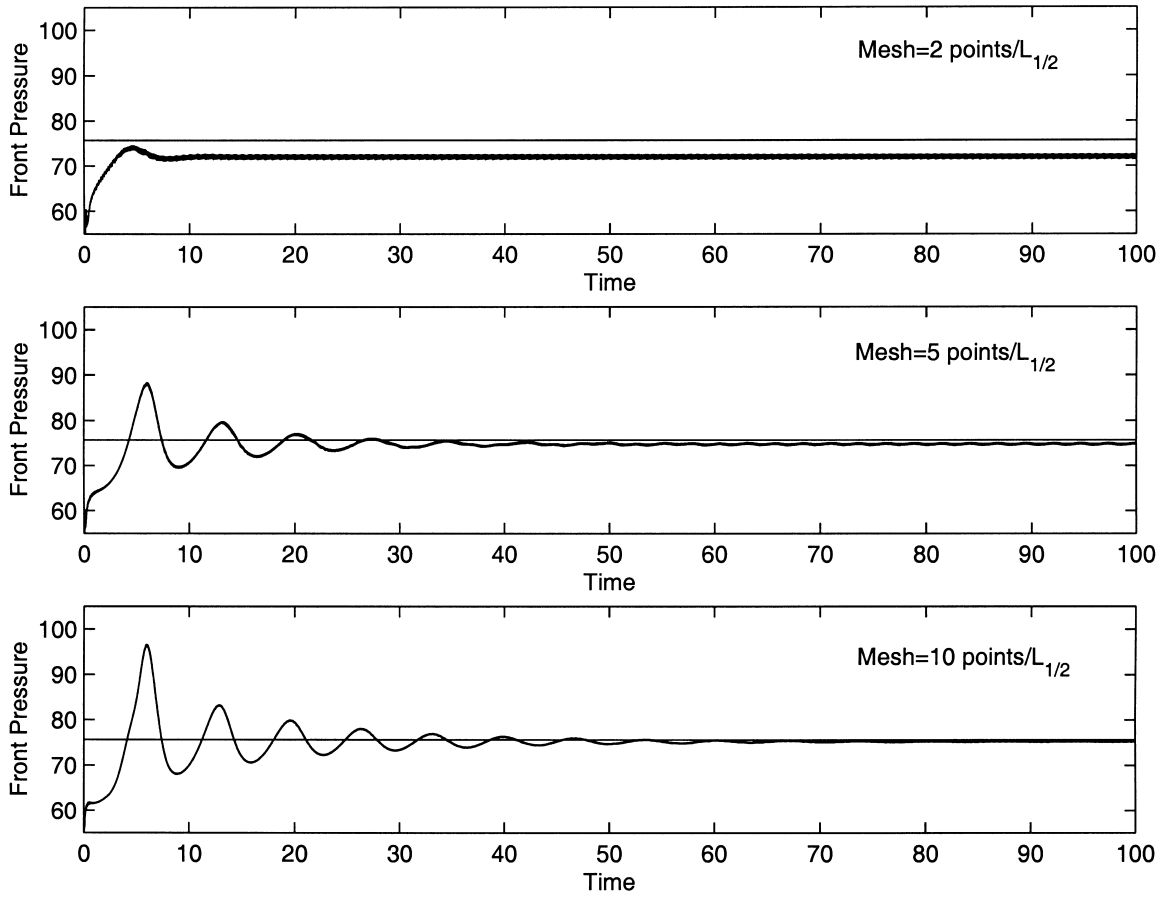

Fig. 4. Mesh refinement study of the shock pressure history for the stable detonative wave, where $f = 1.8$, $Q_0 = E^+ = 50$, $\gamma = 1.2$. (Case 4.4).

4. Numerical examples

In the numerical examples reported in this section, the van Leer limiter is used for the reconstruction of conservative variables W at the beginning of each time step. Except specifically stated, the gas constant γ is equal to 1.4. The first three test cases are about the nonreactive flow and the mass fraction is used as an interface tracer for the fluid evolution; other three test cases are about 1D and 2D detonation wave calculations.

Case 4.1 (Diffusion of mass fraction function)**.** As analyzed in Section 2, the governing equation of the kinetic BGK model for the function ρZ should be the advection diffusion equation,

$$(\rho Z)_t + (\rho U Z)_x = \tau \left(\frac{\rho}{2\lambda} Z_x \right)_x .$$

In order to test the BGK scheme in the description of the above governing equation, we set two uniform initial flow conditions with

$$(\rho = 1, p = 1, U = 0) \quad \text{and} \quad (\rho = 1, p = 1, U = 0.5). \tag{9}$$

The computational domain consists of 200 grid points with cell size $\Delta x = 1.0$. The function Z is initially assigned with the value

$$Z = \begin{cases} -1, & x < 100, \\ 1, & x \geq 100. \end{cases}$$

Two fixed collision times $\tau = 0.03$ and $\tau = 0.015$ are used in the computations, which correspond to viscosity coefficients $\nu = 0.03$ and $\nu = 0.015$, respectively. At the output time $t = 100$, the numerical and exact solutions for both cases are shown in Fig. 1. The results confirm that the BGK scheme do solve the advection diffusion equation for the mass fraction function Z.

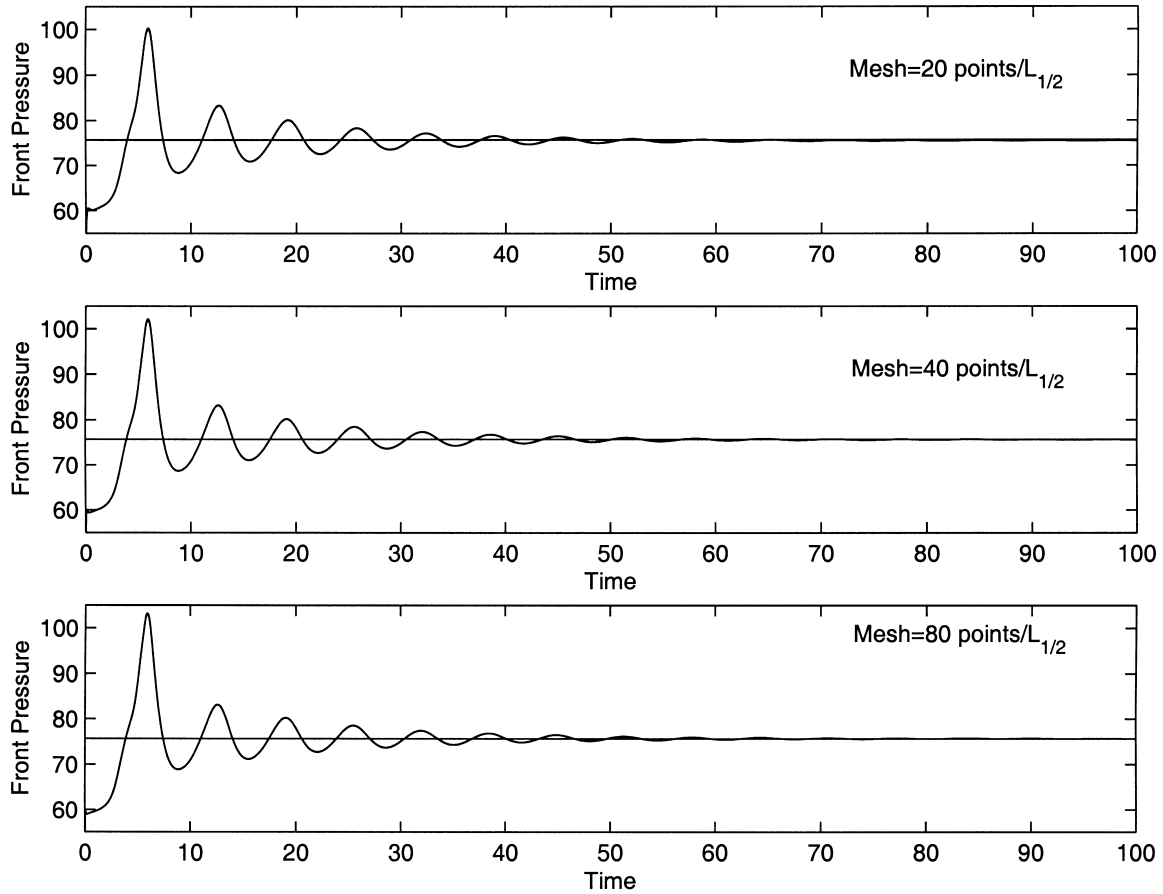

Fig. 5. Mesh refinement study of the shock pressure history for the stable detonative wave with $f = 1.8$, $Q_0 = E^+ = 50$, $\gamma = 1.2$. (Case 4.4).

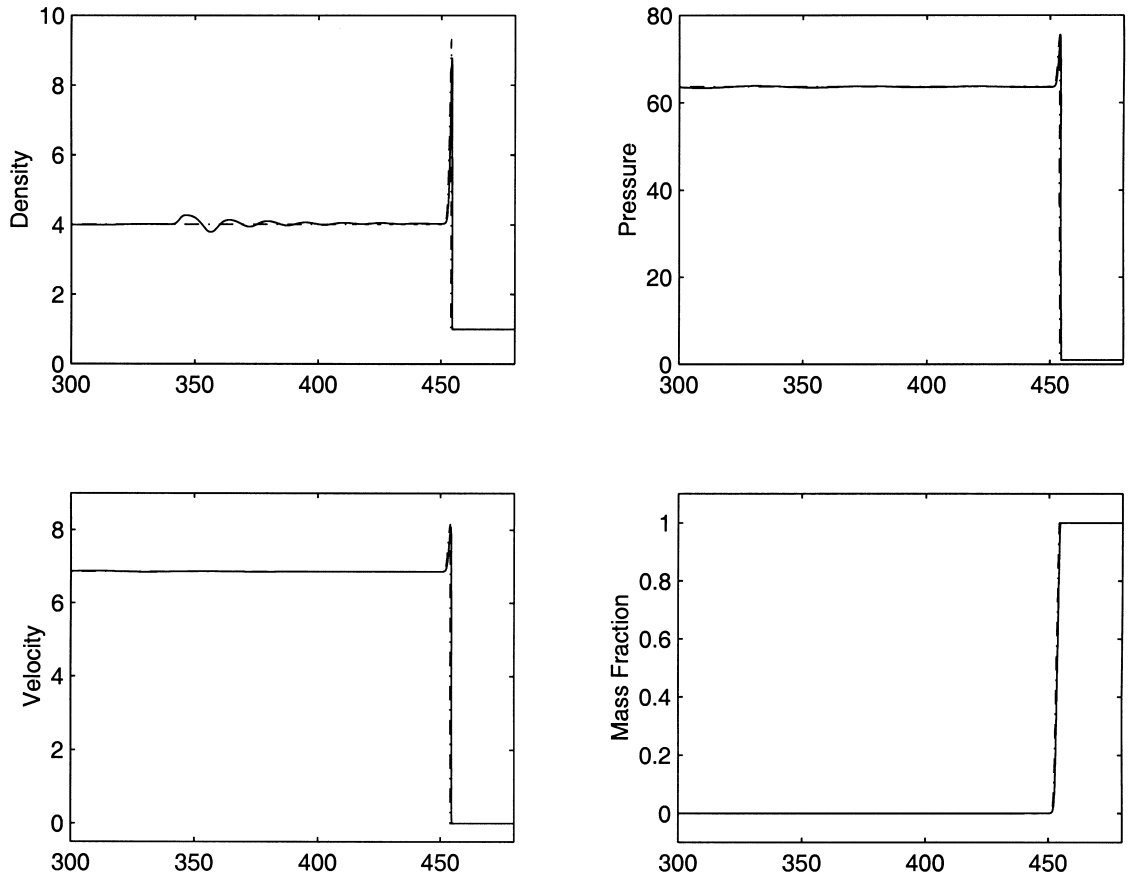

Fig. 6. Numerical solution (solid) of density ρ, velocity U, pressure P and mass fraction Z, where $f = 1.8$, $Q_0 = E^+ = 50$, $\gamma = 1.2$ and 10 points/$L_{1/2}$. The dashed lines are exact solutions. (Case 4.4).

Case 4.2 (Fluid trajectory in the shock tube case [17])**.** The forward-facing step case is carried out on a uniform mesh of 120×40 cells and $\Delta x = \Delta y = 1/40$. We choose the color function Z at the inlet $x = 0$ with the following conditions

$$Z = \begin{cases} 1.0 & \text{for } 0 \le y < \dfrac{3}{40}, \\ -1.0 & \text{for } \dfrac{3}{40} \le y < \dfrac{21}{40}, \\ 1.0 & \text{for } \dfrac{21}{40} \le y < \dfrac{33}{40}, \\ -1.0 & \text{for } \dfrac{33}{40} \le y < 1. \end{cases}$$

The computed density and pressure distributions are presented in Fig. 2. In the same figure, the distributions of function Z are added, from which the interfaces between different 'colored' fluid and the fluid trajectories can be clearly observed. For example, the fluid particles change directions after passing through the oblique shock.

Case 4.3 (Rayleigh–Taylor instability [14,11])**.** This computation is performed on a rectangular domain of $x \in 0, 1$ and $y \in [0, 2]$ with reflecting boundary conditions on the lower and upper sides of the domain and periodic ones in the horizontal direction. The gravity is directed downward with dimensionless gravitational constant $G = 0.5$.

The densities next to the initial fluid interface at $y = 1$ are $\rho_1 = 0.5$ and $\rho_2 = 1.0$ with the ratio $\rho_2/\rho_1 = 2{:}1$, and the functions Z are 1.0 below the interface and -1.0 above that. The value of the pressure at the fluid interface ($y = 1$) is 1/1.4, and isothermal conditions are used separately to determine flow distributions in both the upper and lower parts. The initial density perturbation at the interface is added with the form $\delta\rho = 0.05(1 - \cos(2\pi x))$. Since the heavy fluid is located on top of the light fluid, it stays in an unstable position when the system is

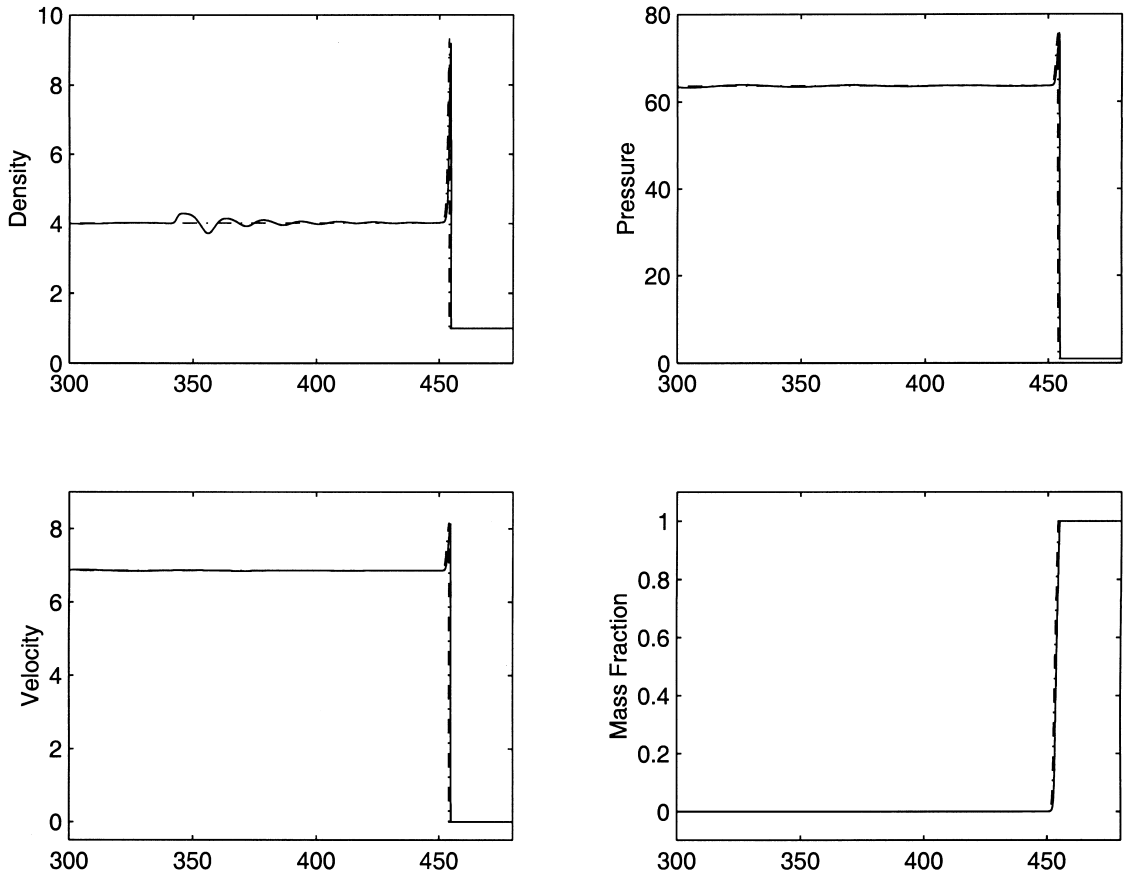

Fig. 7. Numerical solution (solid) of density ρ, velocity U, pressure P and mass fraction Z, where $f = 1.8$, $Q_0 = E^+ = 50$, $\gamma = 1.2$, and 20 points/$L_{1/2}$. The dashed lines are exact solutions. (Case 4.4).

subjected to gravity. The computed function Z with the values $Z = [-0.5, 0.0, 0.5]$ at output time $t = 10.0$ on three different mesh sizes ($\Delta x = \Delta y = 1/64, 1/128, 1/192$) are shown in Fig. 3. Since the collision time $\tau = 4 \times 10^{-4}$ is fixed in all these three cases, the physical viscosity coefficient $\tau p/\rho$ keeps the same value. Therefore, even with the mesh refinement the simulation results are basically identical. If the Riemann solutions of the inviscid Euler equations are used in the flux evaluation $F_{j+1/2}$, the numerical results usually do not converge with the mesh-refinement [14].

In the following, we are going to present the reactive flow calculations. The reaction rate $K(T)$ in Eq. (1) has the following Arrhenius formulation,

$$K(T) = K_0 T^{\alpha} \mathrm{e}^{-E^+/T}, \tag{10}$$

where $\alpha = 0$ is used in the next three cases.

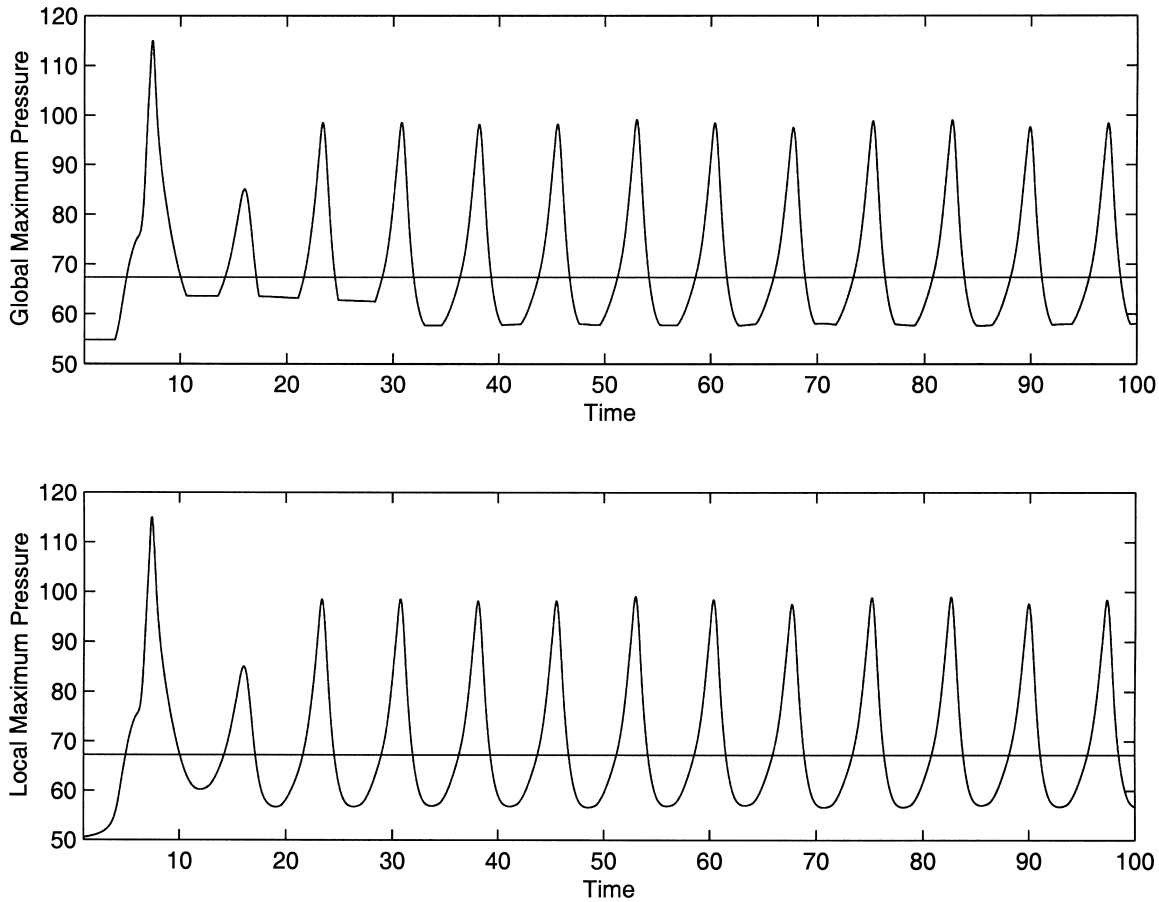

Fig. 8. Plots of (above) the global pressure maxima and (below) the local shock front pressure as a function of time, where $f = 1.6$, $Q_0 = E^+ = 50$, $\gamma = 1.2$, and 80 points/$L_{1/2}$. (Case 4.5).

Case 4.4 (1D stable ZND detonation. $\gamma = 1.2$, $Q_0 = 50$, $E^+ = 50$, $f = 1.8$)**.** This test case is from [2]. The pre-shock state is normalized to be $p_0 = \rho_0 = 1$ and velocity $U_0 = 0$, the post-shock flow distribution are obtained using Chapman–Joguet condition. Since the overdrive factor f is larger than 1.73, the current detonative wave is stable. The prefactor factor K_0 is chosen as $K_0 = 145.68913$, so that the half-reaction length $L_{1/2}$ becomes unit.

According to the results in [8], one of the important requirements in the detonative wave simulation is the spatial resolution. In order to resolve the reaction zone behind the shock wave and get the phase correct, a large computational domain with fine mesh is usually required. For a particular computation, one can be tempted to keep only a few points behind of the shock, with the reasoning that the information behind the shock either never catches up with, or does not affect the shock during the computation. However, if too small a computational domain behind the shock is specified, the points at the edge of and outside of the computational domain cease to be updated after some time into the computation, which leads to a corruption of the data in that region. Hwang et al. [8] pointed out that the

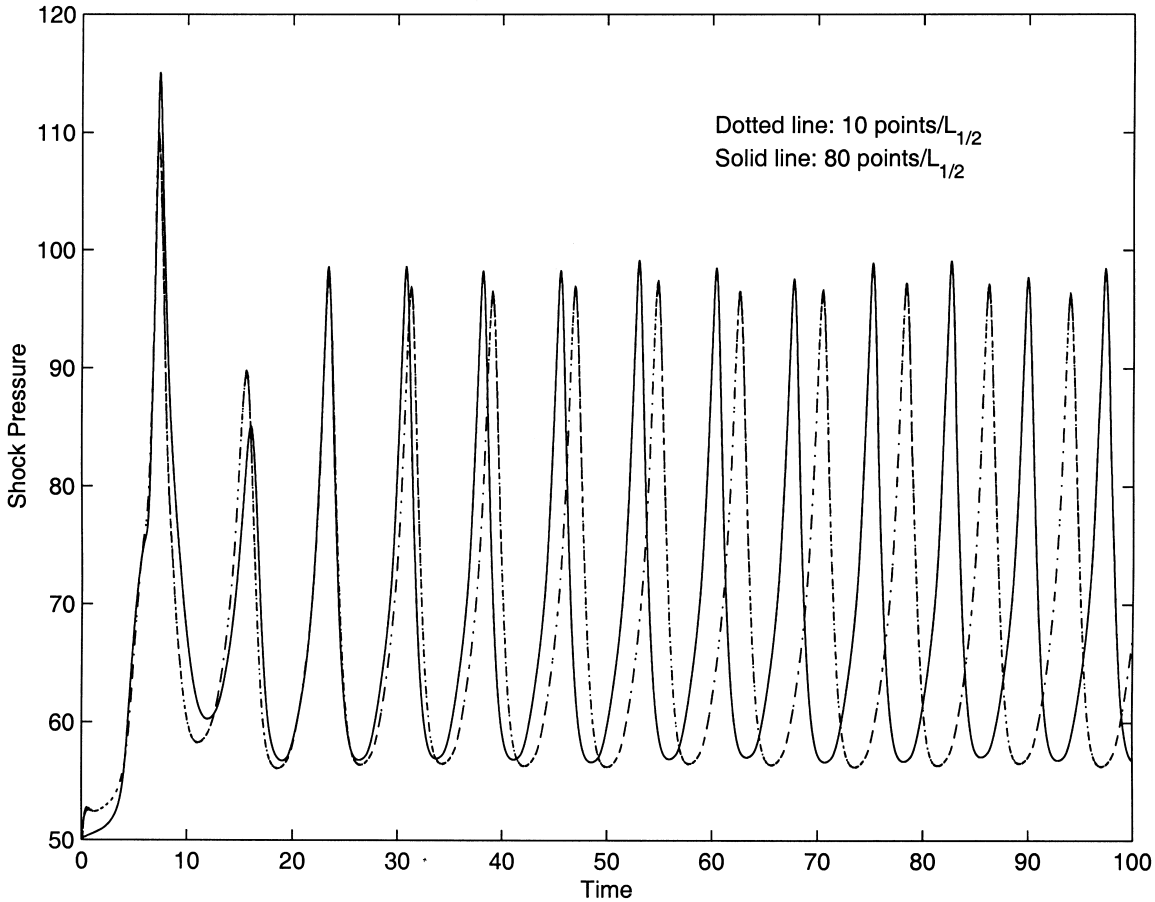

Fig. 9. Local shock pressure as a function of time for the overdriven detonation, where $f = 1.6$, $Q_0 = E^+ = 50$, $\gamma = 1.2$. Dash-dot: 10 points/$L_{1/2}$, solid line: 80 points/$L_{1/2}$. (Case 4.5).

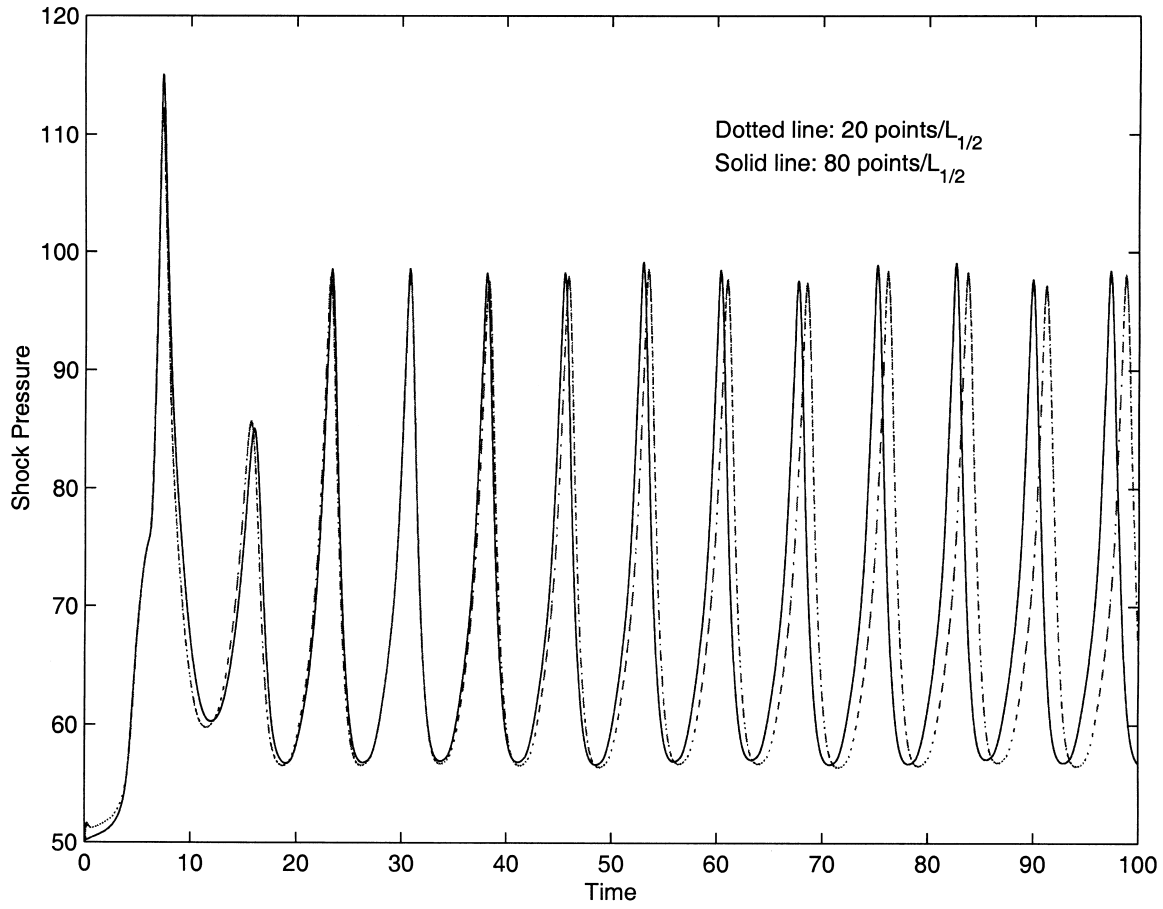

Fig. 10. Local shock front pressure as a function of time for the overdriven detonation, where $f = 1.6$, $Q_0 = E^+ = 50$, $\gamma = 1.2$. Dash-dot line: 20 points/$L_{1/2}$, solid line: 80 points/$L_{1/2}$. (Case 4.5).

computational domain L and time t must satisfy the following inequality

$$t < \frac{L}{U + C - D} + \frac{L}{D}, \tag{11}$$

where D is the speed of shock front, U is the speed of the post-shock flow, and C is the sound speed. In the current calculation, according to the above formulation, L should satisfy

$$L \geq 1.88t.$$

Fig. 4 and Fig. 5 give the numerical shock pressure histories with different mesh size in the current stable ZND wave calculation. On the coarsest mesh (2 points/$L_{1/2}$), the shock pressure is about 5% lower than the theoretical results after time greater than 10. With the mesh 5 points/$L_{1/2}$, even though the results are much improved, the pressure is still about 2% lower

than the analytic value. With the continuous mesh refinement, accurate simulation results can be obtained.

Fig. 6 and Fig. 7 present the distributions of density, velocity, pressure and mass fraction at time $t = 50$. From the above pictures, we can conclude that for the stable problem, 10 points/$L_{1/2}$ is enough to capture the correct ZND structure.

Case 4.5 (1D unstable detonation. $\gamma = 1.2$, $Q_0 = 50$, $E^+ = 50$, $f = 1.6$)**.** This classical unstable detonative wave was first discussed by Fickett and Wood in [7]. An important physical quality for unstable detonation is the pressure history as a function of time at the shock front in a perturbed ZND wave. For a stable ZND wave, the shock pressure history should exhibit small fluctuation about the known precursor shock value and decay with time. In the case of unstable one-dimensional detonation, the shock front pressure history makes larger excursion from the theoretical ZND value due to initial perturbations. For the case with $\gamma = 1.2$,

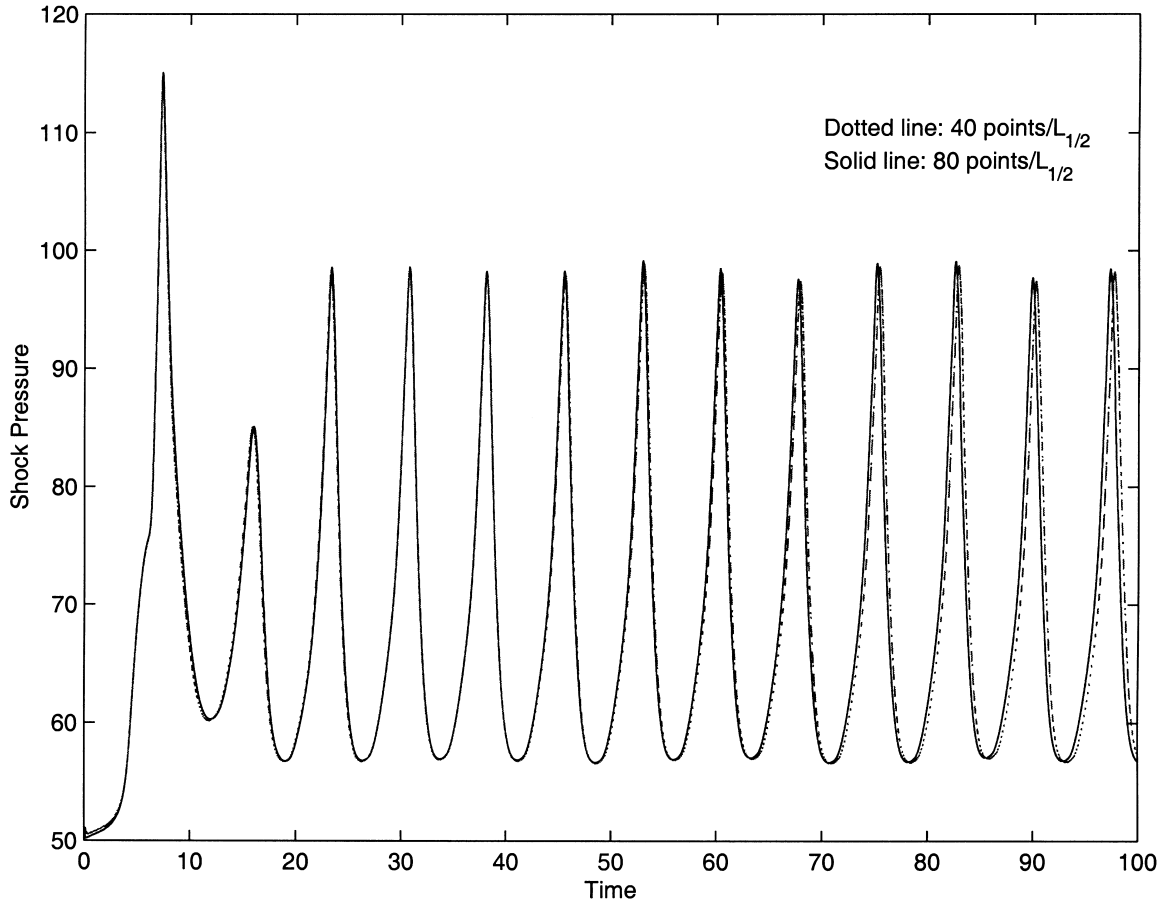

Fig. 11. Local shock front pressure as a function of time for the overdriven detonation, where $f = 1.6$, $Q_0 = E^+ = 50$, $\gamma = 1.2$. Dash-dot line: 40 points/$L_{1/2}$, solid line: 80 points/$L_{1/2}$. (Case 4.5).

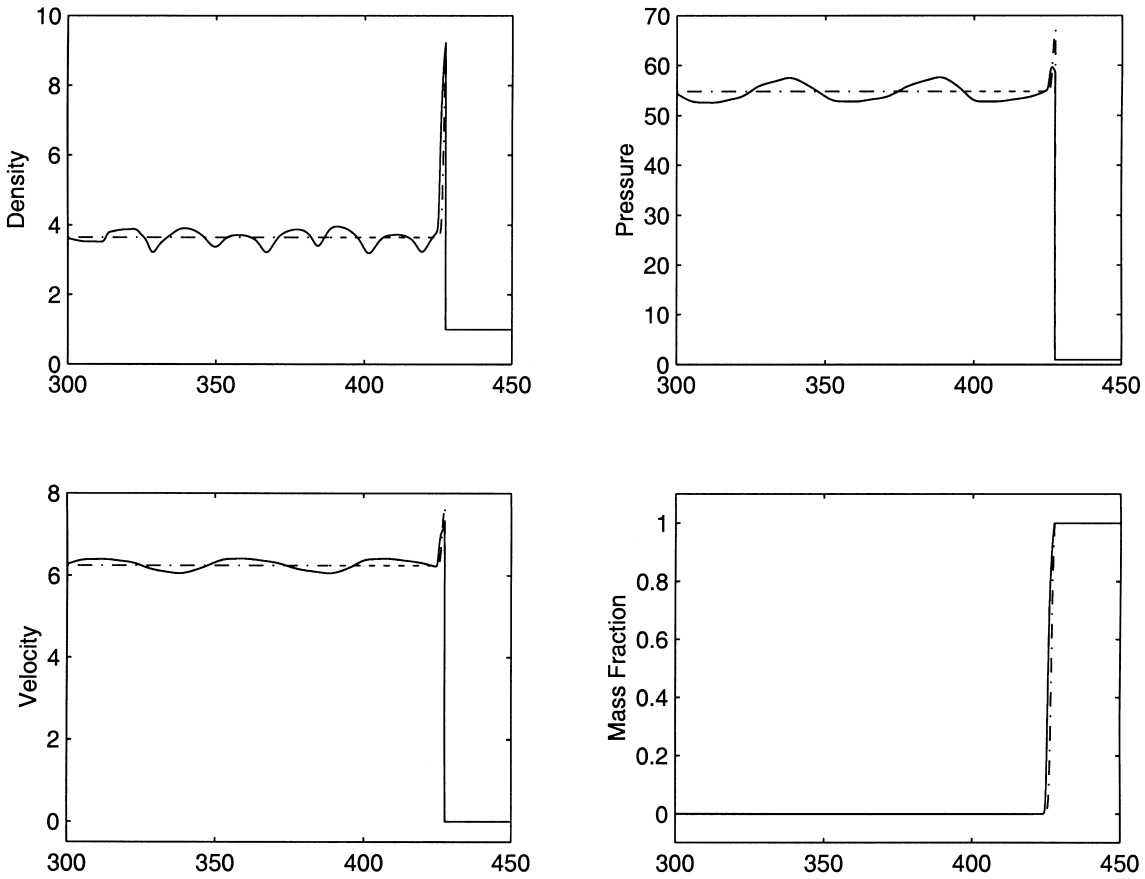

Fig. 12. Numerical unsteady ZND solution (solid) and stable ZND solution (dash-dot) of density, velocity, pressure and mass fraction, where $f = 1.6$, $Q_0 = E^+ = 50$, $\gamma = 1.2$, and 20 points/$L_{1/2}$. The output is at time $t = 50$. (Case 4.5).

$Q_0 = 50$, $E^+ = 50$, and the overdrive $f = 1.6$, Erpenbeck [5] showed that this ZND profile should be a regular periodic pulsating detonation with maximum shock pressure per period given by 101.1 ± 0.2, while the unperturbed ZND shock pressure is about 67.3.

In the current simulation,the density and pressure are normalized to be unit in the pre-shock region. With $Q_0 = 50$ and $\gamma = 1.2$, the dimensionless CJ speed can be obtained with the value $M_{CJ} = 6.80947$. The prefactor K_0 is chosen as $K_0 = 230.75$ so that the length of half-reaction $L_{1/2}$ is equal to unit. The post-shock state is determined by Chapman–Joguet condition with the given dimensionless shock speed M. In the calculation, the so-called 'start-up' error will generate some unexpected phenomena. In Fig. 8, we can see that at about time equal to 8 the shock front pressure amounts to 114. After $t > 15$, the regular pulsating shock front can be obtained.

Fig. 8 shows the global pressure maxima and local shock front pressure as a function of time. This result is obtained with the fine mesh of 80 points/$L_{1/2}$, which can be considered as

the exact solution. The global pressure maxima keeps the same peak value as the local pressure at the shock front. However, the global pressure maxima is higher than the local pressure in the valley of the curve due to the pulsating of the pressure in the post-shock regions (see Fig. 12).

Fig. 9, Fig. 10 and Fig. 11 present the shock front pressure histories with different meshes. On the coarsest mesh (10 points/$L_{1/2}$, Fig. 9), due to the large numerical dissipation, the shock front pressure is about 5% lower than the theoretical results. There is also a great phase difference. Fig. 10 shows an improved results with a fine mesh (20 points/$L_{1/2}$). Still, the pulsation period cannot match well with the exact solution. With the increase of mesh resolution (40 points/$L_{1/2}$), the difference between the numerical and the exact solution reduces, as shown in Fig. 11. Fig. 12 shows the density, velocity, pressure and mass fraction distributions at $t = 50$ with mesh size 20 points/$L_{1/2}$. From this figure, we know that the shock speed is correctly captured. In fact, in terms of shock speed alone, even with a coarser mesh,

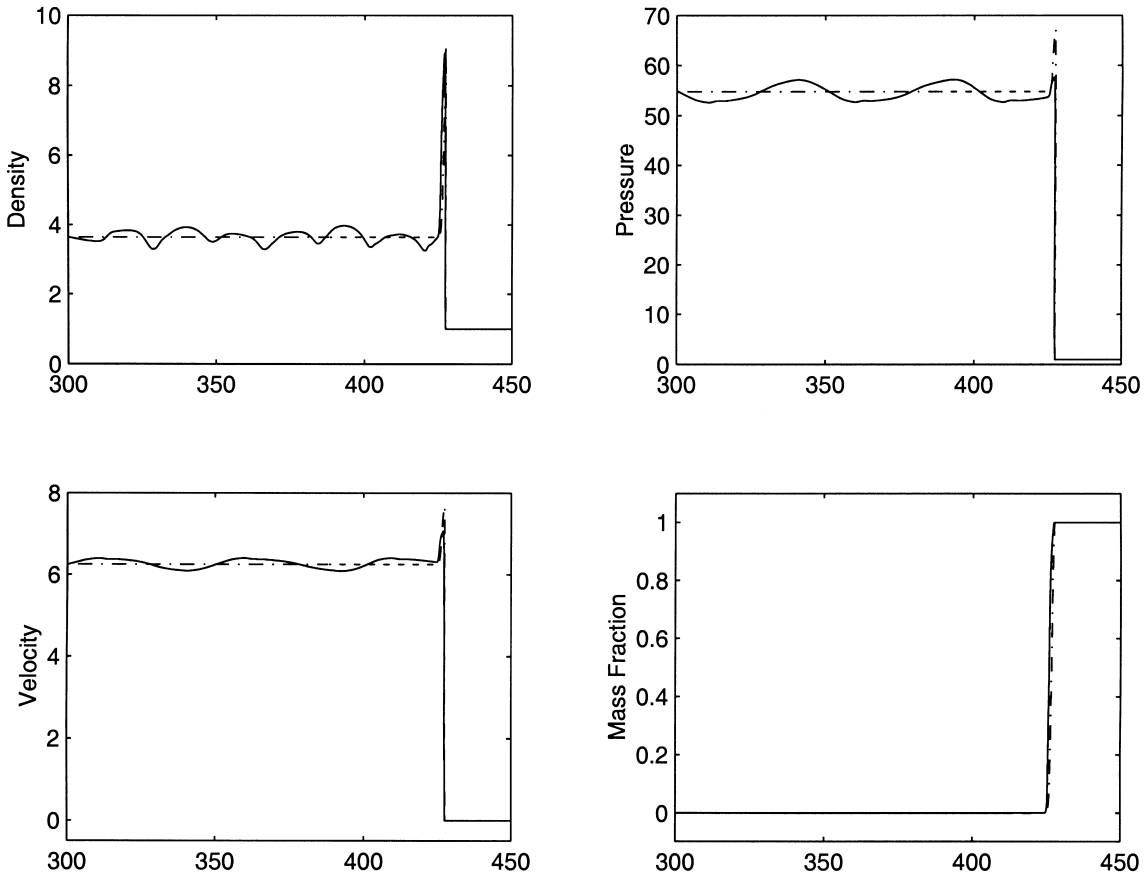

Fig. 13. Numerical unsteady ZND solution (solid) and stable ZND solution (dash-dot) of density, velocity, pressure and mass fraction, where $f = 1.6$, $Q_0 = E^+ = 50$, $\gamma = 1.2$, and 10 points/$L_{1/2}$. The output time is $t = 50$. (Case 4.5).

such as 10 points/$L_{1/2}$, the agreement between numerical and theoretical ones is very well (see Fig. 13). From the simulation result in this case, we can conclude that in order to correctly capture unstable ZND detonative waves, the requirement of 20 points/$L_{1/2}$ is the minimum. Therefore, in the multidimensional case, in order to develop an efficient code, the use of adaptive mesh around the ZND wave front becomes necessary.

Case 4.6 (2D viscous reactive flow)**.** This test case follows [12]. The initial data is a one-dimensional ZND profile in the x-direction. The ZND wave connects the left state $\rho_l = 1.731379$, $U_l = 3.015113$, $V_l = 0$, $\rho_l \epsilon_l = 130.4736$, $Z_l = 0$ by a Chapman–Jouget

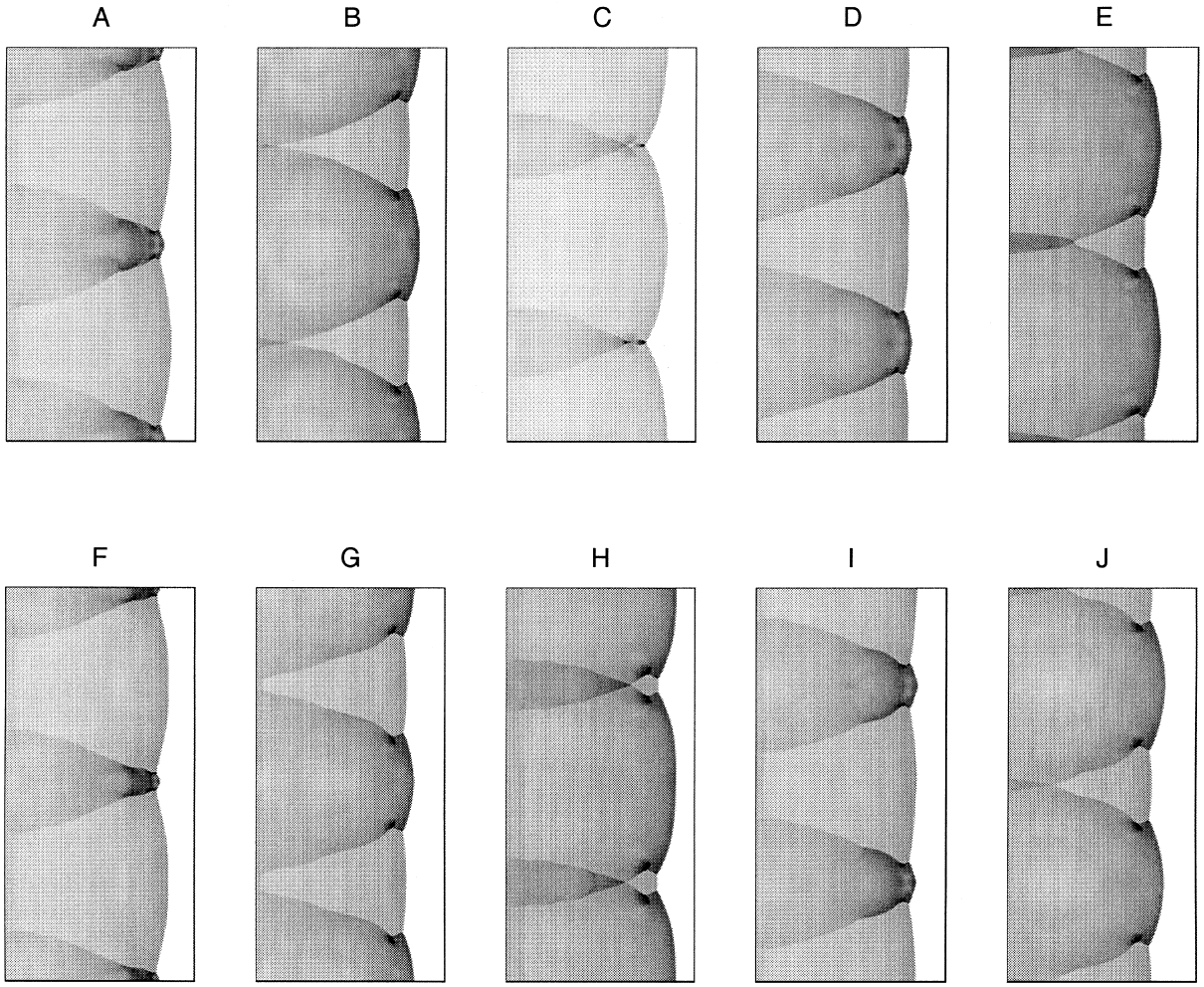

Fig. 14. Sequence of ten snapshots of pressure, where $Q_0 = E^+ = 50$, $\gamma = 1.2$, $\Delta x = \Delta y = \frac{1}{800}$, and 23 points/$L_{1/2}$. Starting from time $t = \frac{13}{80}$, the time increment is $\frac{1}{40}$, and the shock moves rightward. (black = maximum, white = minimum). (Case 4.6).

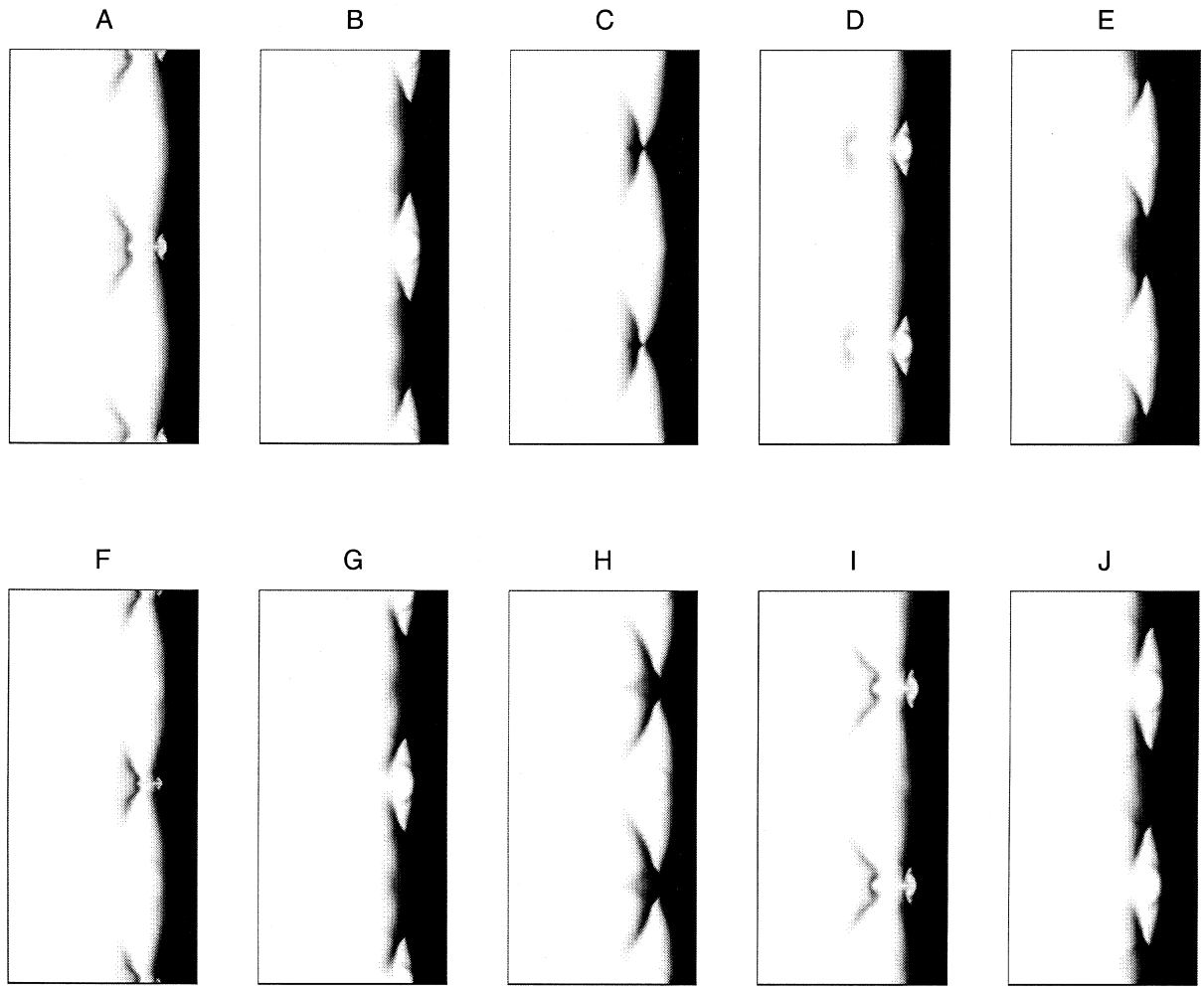

Fig. 15. Sequence of ten snapshots of mass fraction, where $Q_0 = E^+ = 50$, $\gamma = 1.2$, $\Delta x = \Delta y = \frac{1}{800}$, and 23 points/$L_{1/2}$. Starting from time $t = \frac{13}{80}$, the time increment is $\frac{1}{40}$, and the shock moves rightward. (black = maximum, white = minimum). (Case 4.6).

detonation with the right state $\rho_r = 1$, $U_r = 0$, $V_r = 0$, $\rho_r \epsilon_r = 15$, $Z_r = 1$. If no transverse gradient is present in the initial data, the numerical scheme will preserve the one-dimensional structure of the initial flow. So a periodic initial perturbation is imposed in the y-direction of the initial ZND profile, where the initial data $W(x, y, 0)$ is set to $W_{\mathrm{ZND}}(x + \Delta x \mathrm{NINT}(\frac{0.05}{\Delta x}\cos(4\pi y)))$, where NINT(x) is the nearest integer to x.

The flow parameters used in the current case are $Q_0 = E^+ = 50$ and $\gamma = 1.2$. The reaction rate K_0 is set to be 10^4. With the above choice of parameters, the length of half reaction $L_{1/2}$ is equal to 0.0285. The computational mesh size in our case is $\Delta x = \frac{1}{800}$, so there are about 23 points in each $L_{1/2}$. Based on the analysis in [8], it is sufficient to use a domain $x \in [0, 1.2]$ in the current calculation. At the left and the right boundaries, the initial traveling wave solutions

are imposed, and the solid wall boundary conditions are used at the upper and lower boundaries.

Fig. 14 presents a sequence of snapshots of the pressure starting from $t = \frac{13}{80}$, where two triple points just get collided. The shock front is composed of Mach stem, incident shock and reflected shock. The Mach stem portion of the front is very small, but has very high pressure. In the next few snapshots, the motion of triple points, as well as the transverse waves, are presented.

Fig. 15 shows the snapshots of the mass fraction. Before the collision of two triple points, the induction zone formed behind the relatively weak leading shock is large. When the triple

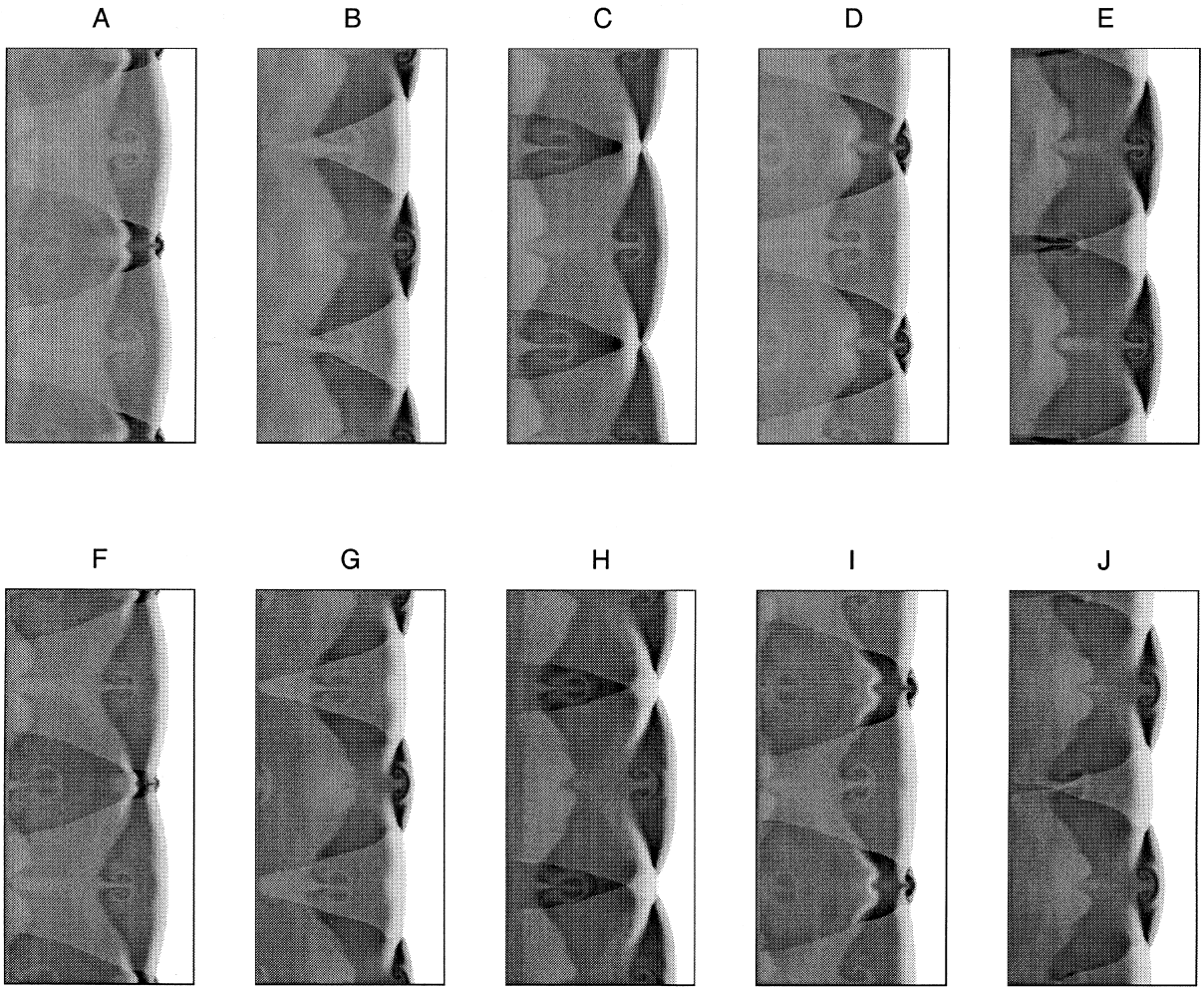

Fig. 16. Sequence of ten snapshots of temperature, where $Q_0 = E^+ = 50$, $\gamma = 1.2$, $\Delta x = \Delta y = \frac{1}{800}$, and 23 points/$L_{1/2}$. Starting from time $t = \frac{13}{80}$, the time increment is $\frac{1}{40}$, and the shock moves rightward. (Black = maximum, white = minimum). (Case 4.6).

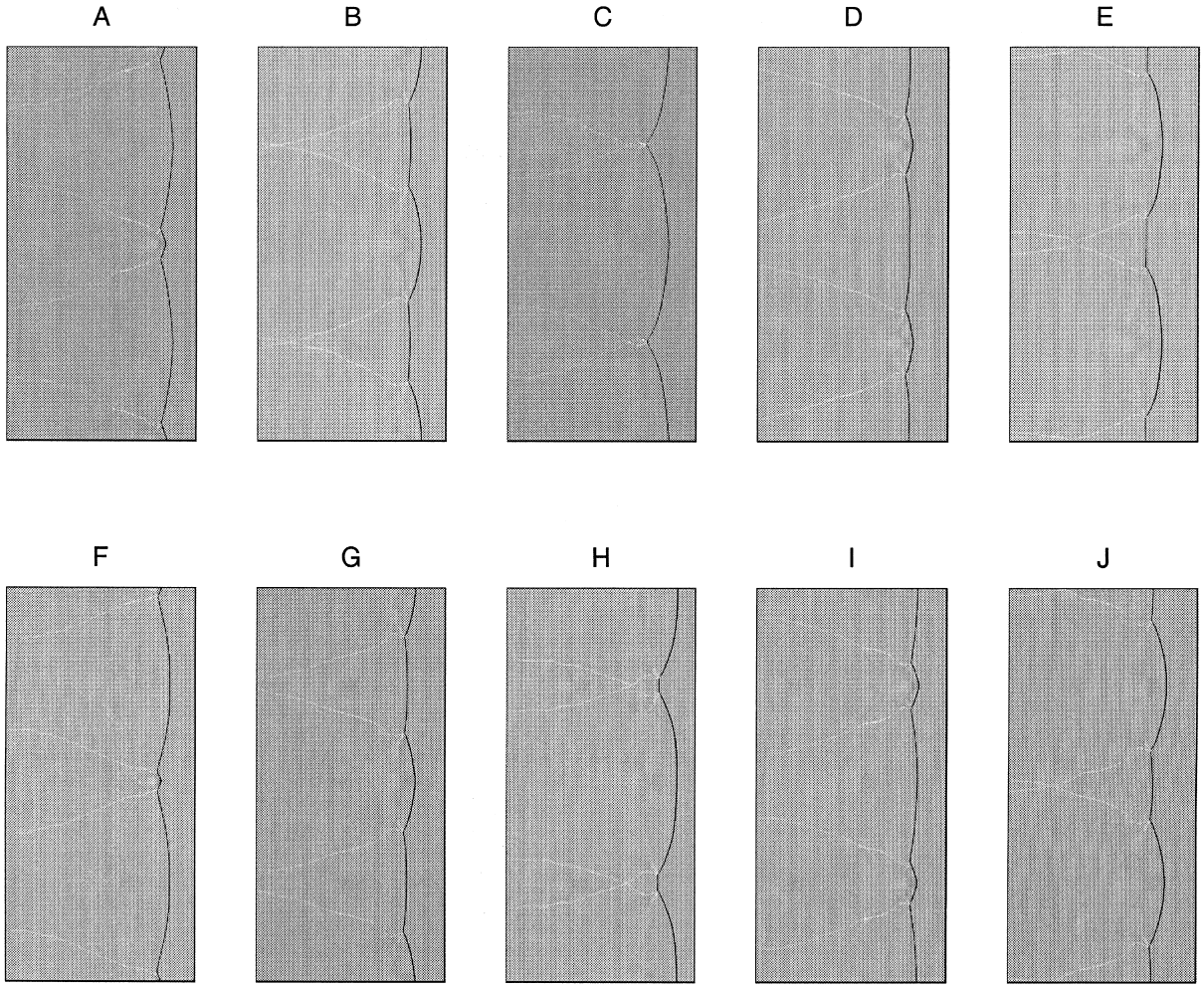

Fig. 17. Sequence of ten snapshots of vorticity, where $Q_0 = E^+ = 50$, $\gamma = 1.2$, $\Delta x = \Delta y = \frac{1}{800}$, and 23 points/$L_{1/2}$. Starting from time $t = \frac{13}{80}$, the time increment is $\frac{1}{40}$, and the shock moves rightward. (Case 4.6).

points collide, this induction zone is cut off and becomes a pocket which moves downstream and gradually disappears as the gas is burnt. Fig. 16 gives the temperature distribution in the whole region. The snapshots of vorticity are shown in Fig. 17.

5. Conclusion

In this paper, we have extended the BGK scheme to the chemical reactive flow. The mass

function is included in the kinetic formulation by assigning a new internal degree of freedom in the gas distribution function. This mass function can be also used to track the fluid interfaces for the nonreactive flows. The numerical results confirm the robustness and accuracy of the BGK method in the description of detonative flow motion.

Acknowledgements

This research was supported in part by the National Aeronautics and Space Administration under NSAS Contract No. NAS1-97046 while the second author was in residence at the Institute for Computer Applications in Science and Engineering (ICASE), NASA Langley Research Center, Hampton, VA 23681-2199. Additional support was provided by Hong Kong Research Grant Council through RGC97/98.HKUST6166/97P.

References

[1] Bhatnagar PL, Gross EP, Krook M. A model for collision processes in gases I: small amplitude processes in charged and neutral one-component systems. Phys Rev 1954;94:511–25.
[2] Bourlioux A. Numerical study of unsteady detonations. PhD Thesis, Princeton University, 1991.
[3] Colella P, Majda A, Roytburd V. Theoretical and numerical structure for reacting shock wave. SIAM J Sci Stat Comput 1986;7(4):1059–80.
[4] Engquist B, Sjogreen B. Robust difference approximations of stiff inviscid detonation waves. Research Report, Computational and Applied Mathematics, UCLA, 1991.
[5] Erpenbeck JJ. Stability of idealized one-reaction detonation. Phys Fluids 1964;7:684–96.
[6] Fickett W, Davis WC. Detonation. Berkeley, CA: University of California Press, 1979.
[7] Fickett W, Wood WW. Flow calculations for pulsating one-dimensional detonations. Phys Fluids 1966;9:903–16.
[8] Hwang P, Fedkiw RP, Merriman B, Karagozian AR, Osher SJ. Numerical resolution of pulsating detonation. UCLA CAM Report 99-12, 1999.
[9] Jeltsch R, Klingenstein P. Error estimators for the position of discontinuities in hyperbolic conservation laws with source terms which are solved using operator splitting. Research Report No. 97-16, ETH, Switzerland, 1997.
[10] Kim C, Jameson A. A robust and accurate LED-BGK solver on unstructured adaptive meshes. J Comput Phys 1998;143:598–627.
[11] Kotelnikov AD, Montgomery DC. A kinetic method for computing inhomogeneous fluid behavior. J Comput Phys 1997;134:364–88.
[12] Lindstrom D. Numerical computation of viscous detonation waves in two space dimensions. Research Report, Department of Scientific Computing, Uppsala University, Uppsala, Sweden, 1996.
[13] Mandal JC, Deshpande SM. Kinetic flux vector splitting for Euler equations. Computers Fluids 1994;23:447–78.
[14] Mulder M, Osher S, Sethian JA. Computing interface motion in compressible gas dynamics. J of Comput Phys 1992;100:209–28.
[15] Pullin DI. Direct simulation methods for compressible inviscid ideal-gas flow. J of Comput Phys 1980;34:231.
[16] Quirk J. Godunov-type schemes applied to detonation flows. ICASE Report 93-15, 1993.
[17] Woodward P, Colella P. Numerical simulations of two-dimensional fluid flow with strong shocks. J Comput Phys 1984;54:115.

[18] Xu K. Gas-kinetic schemes for unsteady compressible flow simulations, 29th CFD Lecture Series, von Karman Institute for Fluid Dynamics, 1998.
[19] Xu K, Kim C, Martinelli L, Jameson A. BGK-based schemes for the simulation of compressible flow. Int J of Comput Fluid Dynamics 1996;7:213–35.